Carbon Nitride Transforms into a High Lithium Storage Capacity Nitrogen-Rich Carbon

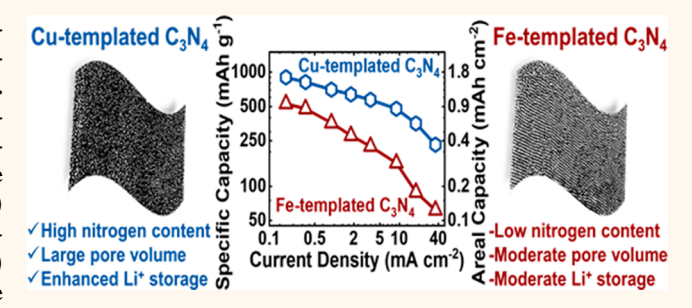
Joshua P. Pender, Doseph V. Guerrera, Bryan R. Wygant, Jason A. Weeks, Ryan A. Ciufo, Blames N. Burrow, Mitchell F. Walk, Mohammad Z. Rahman, Adam Heller, Adam Heller, and C. Buddie Mullins*,†,‡

Department of Chemistry and John J. McKetta Department of Chemical Engineering, The University of Texas at Austin, Austin, Texas 78712, United States

Supporting Information

Downloaded via UNIV OF TEXAS AT AUSTIN on August 28, 2019 at 13:01:01 (UTC). See https://pubs.acs.org/sharingguidelines for options on how to legitimately share published articles.

ABSTRACT: We describe here the metal-templated transformation of carbon nitride (C₃N₄) into nitrogencontaining carbons as anodes for Li-ion batteries (LIBs). Changing the template from the carbon- and nitrogenimmiscible Cu powder to the carbon- and nitrogenmiscible Fe powder yields different carbons; while Fe templating produces graphitized carbons of low (<10%) nitrogen content and moderate pore volume, Cu templating yields high defect-density carbons of high (32-24%) nitrogen content and larger pore volume. The Li⁺ storage capacity of the high nitrogen content and larger pore



volume Cu-templated carbons exceeds that of the more graphitic Fe-templated carbons due to added contribution from Li⁺ insertion/extraction from pores and defects and to reversible faradaic Li⁺ reaction with nitrogen atoms. The Cutemplated carbon annealed at 750 °C delivers the highest specific capacity of 900 mAh g⁻¹ at 0.1 A g⁻¹ and 275 mAh g⁻¹ at 20 A g⁻¹, while also achieving a 96% capacity retention after 2000 cycles at 2 A g⁻¹. The fabrication of higher mass loading electrodes (4.5 mg cm⁻²) provided a maximum areal capacity of 2.6 mAh cm⁻² at 0.45 mA cm⁻² (0.1 A g⁻¹), comparable to the capacities of commercial LIB cells and favorable compared to other reported carbon materials.

KEYWORDS: carbon nitride, lithium-ion battery, nitrogen-doped carbon, anode, rate capability, energy storage

i-ion batteries (LIBs) have emerged as the battery of choice in applications spanning from portable electronics to electric vehicles and grid storage owing to their superior energy density per unit weight and volume compared to other battery systems. 1-5 Still, the demands for future applications require LIBs with higher energy density, longer cycle life, and/or lower cost than current state-of-the-art devices. These challenges have motivated significant research into developing new materials that store more Li+ per weight and volume than the conventional graphite anode (capacity \sim 370 mAh g⁻¹) and layered transition-metal oxide cathode (e.g., Li[Ni_xCo_yMn_z]O₂; capacity \sim 180 mAh g⁻¹).³⁻⁹ As the cathode is currently the limiting factor in LIB cells, increasing the weight fraction of the cathode active material provides a direct route to increasing the cell-level energy density. 4,7,10-14

One way of achieving higher energy density involves replacing the standard graphite anode with a higher capacity material that would reduce the required anode loading to match the cathode capacity and thus increase the cathode weight fraction at the cell level.^{3,9} Of the high-capacity materials proposed, 15-18 heteroatom-doped carbons have recently emerged as potentially useful, having low-cost

precursors, tunable surface and structural properties through synthesis optimization, and enhanced electrochemical properties compared to undoped carbon. 19,20 The inclusion of B, N, S, P, etc., defects into carbon architectures has been postulated to enhance their electrochemical performance compared to undoped carbons by increasing the number of electrochemically active sites and facilitating charge transfer between the electrolyte and electrode surface. Importantly, in the most common nitrogen-doping strategy, the enhancement in performance is dependent not only on the overall atomic nitrogen incorporation but also on the bonding environment of the resulting nitrogen functionalities. 21,27,32 Controlling these parameters is thus important in designing high-performance materials, and identifying requisite materials and processing methods has drawn significant research attention.³³⁻³⁷

X-ray photoelectron spectroscopic (XPS) studies on nitrogen-doped carbons commonly identify the following four major bonding configurations between nitrogen and carbon

Received: May 18, 2019 Accepted: August 7, 2019 Published: August 7, 2019

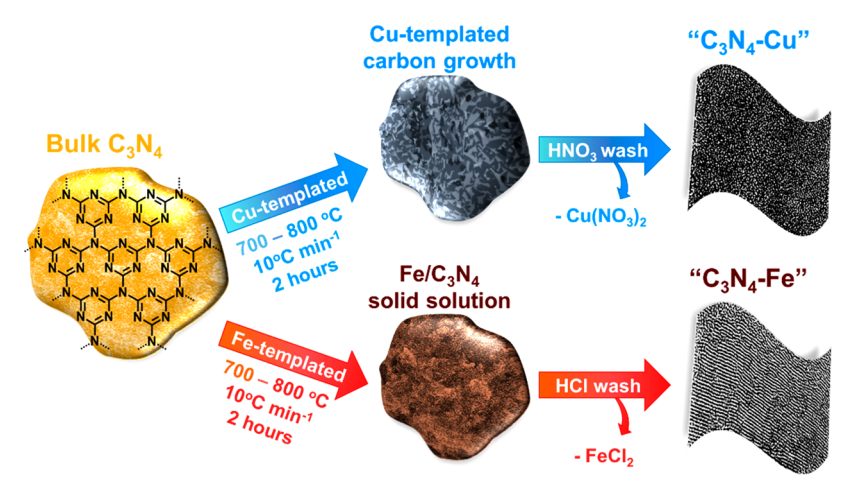


Figure 1. Schematic illustration of the Cu-templated (top, " C_3N_4 -Cu") and Fe-templated (bottom, " C_3N_4 -Fe") transformation of bulk C_3N_4 into nitrogen-doped carbons.

atoms: (1) pyridinic-N (-C = N - C; 398.1-398.5 eV); (2) pyrrolic-N (C - NH - C; 399.8-400.5 eV); (3) graphitic or quaternary-N ($C_3 - N$; 401.1-402.7 eV); and (4) oxidized pyridinic-N ($C_2 - N^+ - O_x^-$; 403-405 eV). $^{34,38-41}$ The different hybridization of the respective nitrogen functionalities affects the electronic properties of carbons in different ways, and thus their relative abundance strongly influences the suitability of a nitrogen-doped carbon for a given application. 33,34

In the case of Li⁺ storage, the sp²-hybridized pyridinic-N and pyrrolic-N groups that primarily occur at edge sites of carbon layers are believed to be most favorable, while graphitic-N are postulated to bind irreversibly with Li+ and degrade cyclability. 19,32 A first-principles study conducted by Ma et al. on the impact of different nitrogen functionalities on Li+ storage in nitrogen-doped graphene nanosheets predicted that pyridinic-N and pyrrolic-N groups provided both (1) the largest increase in the average Li-Li distance upon lithiation and (2) the strongest binding energies with Li⁺ that minimize Li-Li cluster formation and enable higher Li+ storage capacities.²¹ Interestingly, the most competitive Li⁺ storage metrics of greater than 1200 mAh g⁻¹ (at low current density and low (or in some cases, not reported) active-material loading) have been reported for nitrogen contents in the range of ~5-20%; This variation likely stems from differences in surface area and pore structure that control the electrodeelectrolyte contact area and the number of accessible Li⁺ storage sites. Thus, the Li⁺ storage properties of nitrogendoped carbons rely on both their surface chemistry and textural properties.22

In search of suitable nitrogen-doped carbon precursors, carbon nitride, C_3N_4 , is attractive owing to its ease of synthesis by heating low-cost precursors such as urea, melamine, or dicyandiamide to above 525 °C, high structural N content (57% atomic N), and easily discernible fingerprint features by X-ray diffraction (XRD). ³³ Pristine C_3N_4 is, however, a poor electrical conductor ($\sim 10^{-5}$ S cm $^{-1}$) and has a low specific surface, typically <60 m² g $^{-1}$, limiting its utility in energy storage applications. ^{25,32,33,37,51} Former studies have explored tuning the electronic and textural properties of C_3N_4 *via* templating, physical exfoliation, salt melts, and heteroatom and/or transition-metal doping. ^{25,51–55} The majority of these efforts have focused on photocatalytic and electrocatalytic applications rather than on the enhancement of their Li⁺ storage capacity. ^{23,25,30,31}

The theoretical Li⁺ storage capacity for bulk C_3N_4 was first predicted in 2014 in a first-principles study to be 1165 mAh g^{-1} , assuming the reversible $C_3N_4 + 4$ Li⁺ + 4 e⁻ \leftrightarrow Li₄ C_3N_4 reaction. However, merely 200 mAh g^{-1} with poor cycle stability was achieved. Chen and co-workers annealed bulk C_3N_4 with Mg powder at 750 °C under a N_2 atmosphere, chair denitrogenating the C_3N_4 by forming Mg₃N₂, reducing the nitrogen content from 51% to about 9% while increasing the Brunauer–Emmett–Teller (BET) surface area from 60 m² g⁻¹ to 590 m² g⁻¹. The performance of the resulting carbon resembled that of other high-performance nitrogen-doped carbons. Overall, tuning of the Li⁺ storage properties of C_3N_4 -derived carbons has thus far been little explored.

Here, we transform bulk $\mathrm{C_3N_4}$ into nitrogen-doped carbons with varying nitrogen content and pore characteristics by their templating with Cu or Fe powder and annealing at 700–800 °C under Ar. We use poorly carbon- and nitrogen-alloying Cu powder as a model of templating with an immiscible metal and Fe powder as a model of templating with a carbon- and nitrogen-alloying metal. The very different alloying changes the carbon-growth process that provides carbons with different physiochemical and Li^+ storage characteristics.

RESULTS AND DISCUSSION

Synthesis and Characterization of C_3N_4 -Derived Nitrogen-Doped Carbons. The following shorthand terms are used throughout: In C_3N_4 -Mxxx, M refers to the templating metal, Cu or Fe; and xxx refers to the annealing temperature (700, 750, or 800 °C). For example, C_3N_4 -Cu700 means C_3N_4 annealed with Cu powder at 700 °C, and C_3N_4 -Fe800 means C_3N_4 annealed with Fe powder at 800 °C.

Bulk C₃N₄ was synthesized by the commonly reported thermal condensation of urea at 550 °C for 4 h.³³ The carbons were obtained by annealing the bulk C₃N₄ at 700–800 °C under Ar with Cu powder (Figure 1, top) or Fe powder (Figure 1, bottom) followed by acid washing to remove Cu and Fe co-products. Figure 2 displays representative scanning electron microscopy (SEM) images of the precursor materials (Figure 2a–c, left column) and the resulting Cu-templated (Figure 2d–f, middle column with increasing annealing temperature from top to bottom) and Fe-templated (Figure 1g–i, right column with increasing annealing temperature from top to bottom) carbons obtained from the process illustrated in Figure 1. Significant changes in morphology are observed

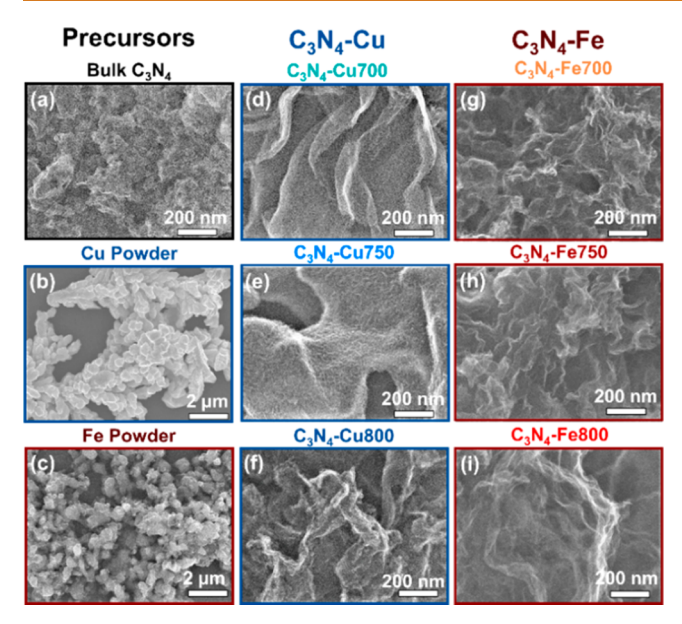


Figure 2. Scanning electron micrographs (SEM) of (a) bulk C_3N_4 , (b) Cu powder, and (c) Fe powder used as precursor materials (left column). (d-f) C_3N_4 -Cu carbons produced at different annealing temperatures (middle column, increasing temperature from top to bottom). (g-i) C_3N_4 -Fe carbons produced at different annealing temperatures (right column, increasing temperature from top to bottom).

following reaction of bulk C_3N_4 (Figure 2a and Figure S1), and these changes appear dependent on both metal precursor and annealing temperature. While Cu templating produces carbons with rough surfaces and temperature-dependent morphological features (Figure 2d–f, middle column; additional SEM images in Figure S2), the C_3N_4 -Fe carbons (Figure 2g–i, right column) possess a wrinkled, sheet-like morphology that stays consistent with increasing annealing temperature (top to bottom in right column), and their surfaces appear smoother compared to the C_3N_4 -Cu samples (additional SEM images of C_3N_4 -Fe carbons in Figure S3).

The morphological differences induced by changing the alloying process are further demonstrated by high-resolution transmission electron microscopy (HR-TEM) images of the nitrogen-doped carbon samples obtained at 750 °C shown in Figure 3. Similar to previous reports, the bulk C₃N₄ (Figure 3a) possesses a bulky sheet-like morphology with a high degree of porosity. Following Cu templating, the C₃N₄-Cu750 carbon (Figure 3b) shows little long-range structural ordering with an abundance of micro/mesopores, whereas the Fetemplated C₃N₄-Fe750 carbon (Figure 3c) possesses an ordered, graphite-like structure with little evidence of additional mesopore formation. The SEM (Figure 2) and HR-TEM (Figure 3) results suggest that the choice of metal template directly influences both the structural and textural properties of C₃N₄-derived nitrogen-doped carbons.

Figure 4 shows powder XRD patterns of the bulk C_3N_4 and metal-templated carbons. The XRD pattern of bulk C_3N_4 in Figure 4a shows the two common features of C_3N_4 materials that correspond to (1) in-plane repeats of heptazine (C_6N_7) units $(2\theta = 12.8^\circ$, d-spacing = 6.91 Å) and $(2) \pi - \pi$ stacking of the C_6N_7 on top of one another $(2\theta = 27.5^\circ$, d-spacing = 3.24 Å). Following Cu templating, the C_3N_4 -Cu carbons (Figure 4b) exhibit broad peaks in the range $2\theta = 25.9-26.7^\circ$. Increasing the annealing temperature from 700 °C $(C_3N_4-1.5000)$

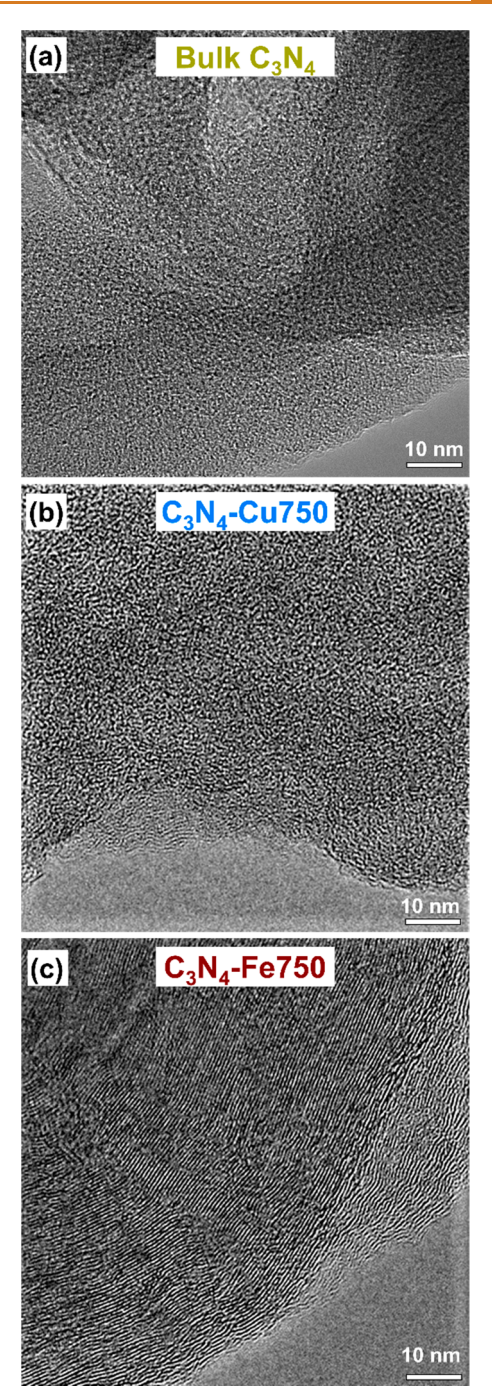


Figure 3. Representative HR-TEM images comparing the nanostructure of (a) bulk C_3N_4 , (b) C_3N_4 -Cu750, and (c) C_3N_4 -Fe750.

Cu700, Figure 4b bottom trace) to 750 °C (C_3N_4 -Cu750, Figure 4b middle trace) increases the interlayer distance from 3.34 to 3.44 Å, but this trend reverses at 800 °C (C_3N_4 -Cu800, Figure 4b top trace) with a decrease in d-spacing to 3.36 Å. We speculate that this trend is likely a result of increasing order in the carbon architecture when the annealing temperature is increased from 750 °C to 800 °C. In contrast, increasing the annealing temperature above 700 °C with Fe results in graphitic-like carbon with a sharp peak at $2\theta = 26.3 - 26.4$ ° (d-spacing = 3.38–3.39 Å) for C_3N_4 -Fe750 (Figure 4c, middle trace) and C_3N_4 -Fe800 (Figure 4c, top trace).

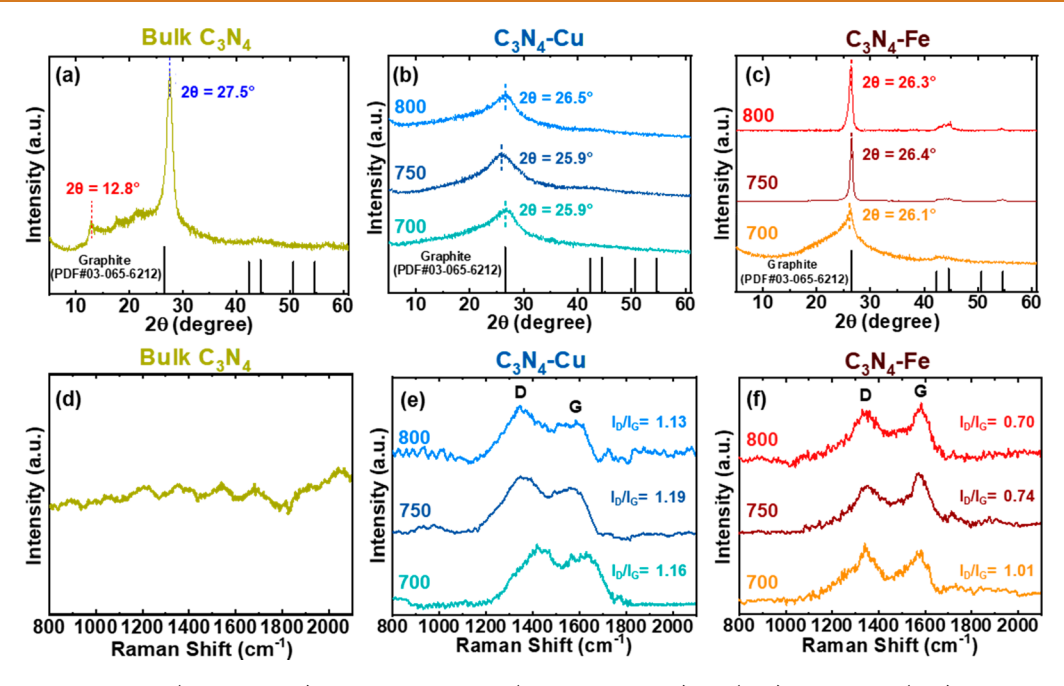


Figure 4. Powder XRD patterns (a-c, top row) and Raman spectra (d-f, bottom row) for (a, d) bulk C_3N_4 , (b, e) C_3N_4 -Cu carbons, and (c, f) C_3N_4 -Fe carbons.

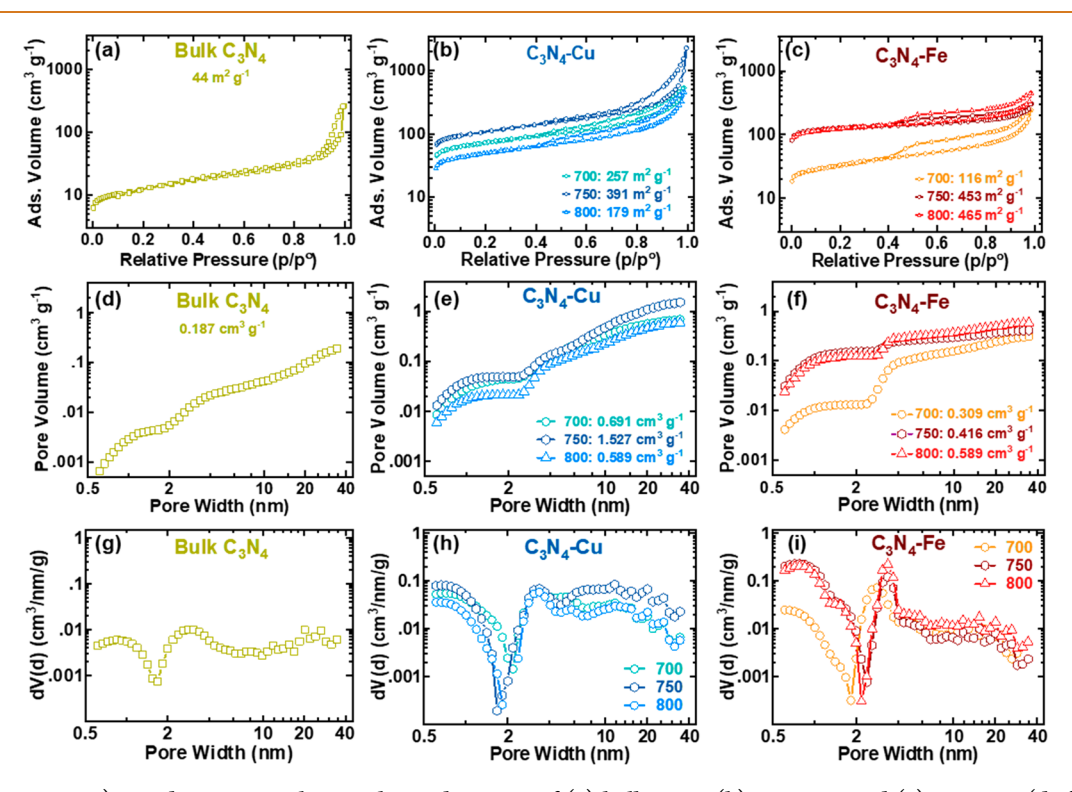


Figure 5. (a-c, Top row) N_2 adsorption isotherms obtained at 77 K of (a) bulk C_3N_4 , (b) C_3N_4 -Cu, and (c) C_3N_4 -Fe. (d-f, Middle row) Cumulative pore volumes derived from N_2 isotherms using quenched solid density functional theory (QSDFT) of (d) bulk C_3N_4 , (e) C_3N_4 -Cu, and (f) C_3N_4 -Fe. (g-i, Bottom row) QSDFT-derived pore-size distributions of (g) bulk C_3N_4 , (h) C_3N_4 -Cu, and (i) C_3N_4 -Fe.

The structural changes of bulk C_3N_4 induced by Cu and Fe templating were further elucidated by Raman spectroscopy (Figure 4d–f). While the bulk C_3N_4 (Figure 4d) showed no significant Raman features, the appearance of two distinct features in the 1300-1600 cm⁻¹ region of the C_3N_4 -Cu (Figure 4e) and C_3N_4 -Fe (Figure 4f) Raman spectra is consistent with the well-known D- and G-bands of graphite/graphene materials and confirms the transformation of C_3N_4

into carbon materials. The G-band in the region of 1570–1610 cm⁻¹ corresponds to sp²-hybridized carbon, whereas the D-band in the lower frequency region of 1340–1380 cm⁻¹ is activated by defects present in a carbon architecture; comparing the relative intensities of the D- and G-band ($I_{\rm D}/I_{\rm G}$ ratio) therefore provides insight into the defect density in carbon materials. The broadness of the D-band and G-band observed for all of the carbon samples indicates

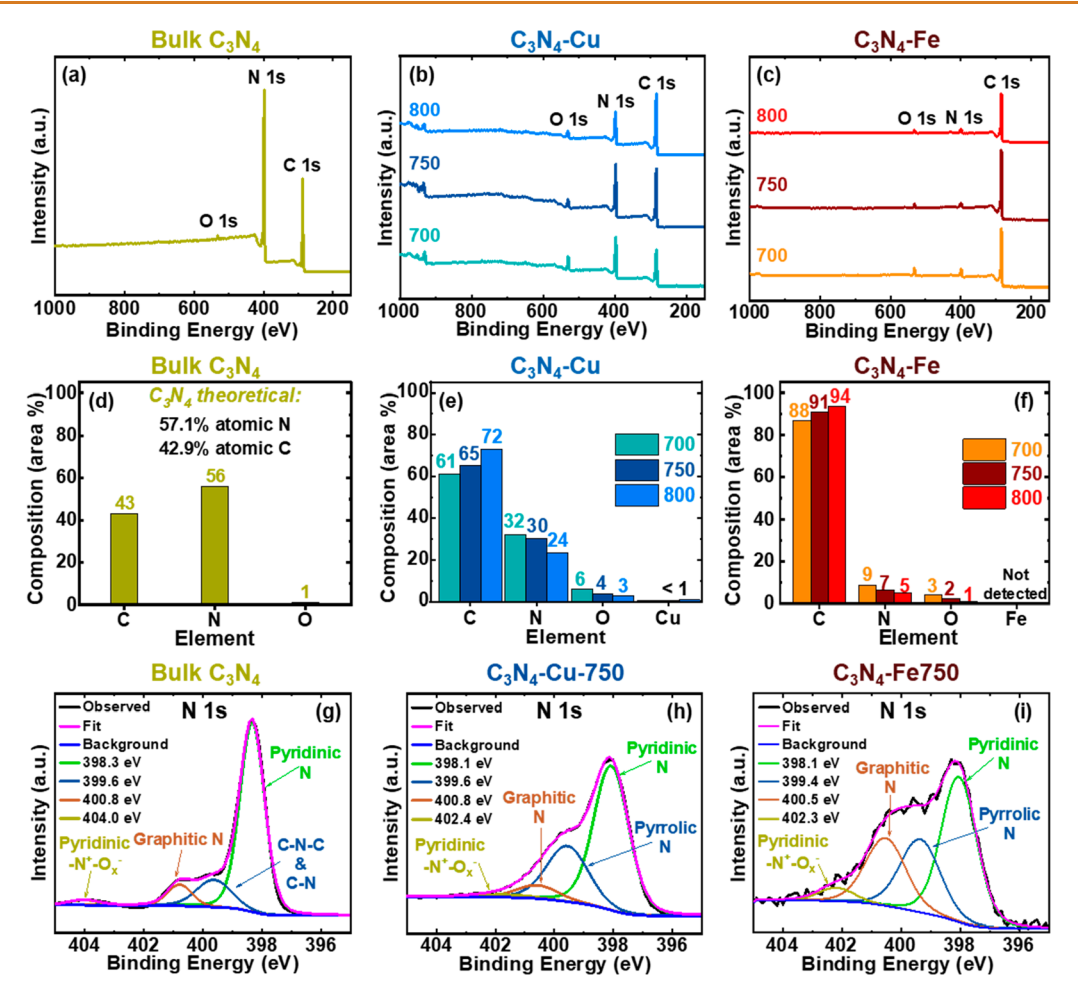


Figure 6. X-ray photoelectron spectroscopy (XPS) survey scans of (a) bulk C_3N_4 , (b) C_3N_4 -Cu carbons, and (c) C_3N_4 -Fe carbons. Atomic compositions calculated by comparing the fractional area of deconvoluted high-resolution XPS spectra for (d) bulk C_3N_4 , (e) C_3N_4 -Cu, and (f) C_3N_4 -Fe at different annealing temperature. High-resolution N 1s spectra for (g) bulk C_3N_4 , (h) C_3N_4 -Cu750, and (i) C_3N_4 -Fe750.

the presence of other defect-activated peaks, and thus the Dand G-bands for the C₃N₄-Cu (Figure S4 and Table S1) and C₃N₄-Fe (Figure S5 and Table S2) were deconvoluted by fitting the spectra using a Voigt function (convolution of Gaussian and Lorentzian functions) to determine the I_D/I_G ratio.⁵⁴ The C₃N₄-Fe carbons show trends consistent with previous reports of higher structural ordering with increasing annealing temperature, evidenced by a decrease in the I_D/I_G ratio at higher annealing temperature (Figure 4f). 30,34,42 The low I_D/I_G values of 0.74 for C_3N_4 -Fe750 and 0.70 for C_3N_4 -Fe800 support the TEM (Figure 3b) and XRD (Figure 4c) analyses that show significant structural order in the Fetemplated carbons compared to the analogous Cu-templated carbons. Not only are the C₃N₄-Cu carbons more defective, but an interesting trend emerges in the determined I_D/I_G values of 1.16, 1.19, and 1.13 at 700, 750, and 800 °C, respectively (Figure 4e). Understanding the curious trend from 700 to 750 °C during Cu templating requires further investigation, as the relative intensities of the D-band and Gband can be influenced by both chemical defects (e.g., heteroatom-doping) and physical/textural defects (e.g., pores and surface roughness).54,5

The specific surface areas and pore characteristics of the bulk C_3N_4 , C_3N_4 -Cu carbons, and C_3N_4 -Fe carbons obtained from 77 K N_2 adsorption isotherms are shown in Figure 5. All exhibit IUPAC type IV isotherms with an H4-type hysteresis in

the p/p° of 0.4–1.0, which are characteristic of materials with both micro- and mesoporosity.^{25,58-60} Consistent with previous reports on bulk C₃N₄, BET analysis shows highly mesoporous character with a low specific surface area (44 m² g⁻¹, Figure 5a). ^{25,32,33,37,51} Following Cu templating and annealing at 700 °C, the BET surface area of the C₃N₄-Cu700 carbon increases nearly 6-fold to 257 m² g⁻¹ (Figure 5b, teal isotherm) compared to the bulk sample and further increases to 391 m 2 g $^{-1}$, about 9 times the BET surface area of bulk C_3N_4 , at 750 °C (Figure 5b, navy isotherm). However, increasing the annealing temperature further to 800 °C results in a 54% decrease in BET surface area for the C_3N_4 -Cu800 carbon compared to that at 750 °C (Figure 5b, light blue isotherm). Examination of the pore volume derived from the N₂ adsorption isotherms using quenched solid density functional theory (QSDFT) for the C₃N₄-Cu carbons shows contributions from both micro- and mesopores (Figure 5e). Notably, a large increase in pore volume from 0.691 cm³ g⁻¹ for C₃N₄-Cu700 (Figure 5e, teal circles) to 1.527 cm³ g⁻¹ for C₃N₄-Cu750 (Figure 5e, navy hexagons) and the pore-width mode increase nearly 3.5 times from 3.4 nm for C₃N₄-Cu700 to 11.8 nm for the C₃N₄-Cu750 carbon (Figure 5h). The C₃N₄-Cu750 carbon thus has both the highest BET surface area and largest pore volume, both of which are favorable for increasing the Li^+ storage capacity. 22,25,31,61

Table 1. Surface Nitrogen Content and Nitrogen Functionalities (Pyridinic-N, Pyrrolic-N, Graphitic-N, and Pyridinic-N $^+$ -O $_x$ ⁻) of C₃N₄-Derived Carbons by XPS (C₃N₄-Cu: Figure 6h and Figure 87; C₃N₄-Fe: Figure 6i and Figure 88)

sample	surface nitrogen content (%)	pyridinic-N(398.2 \pm 0.1 eV) (fractional %)	pyrrolic-N(399.5 \pm 0.1 eV) (fractional %)	graphitic-N(400.7 \pm 0.3 eV) (fractional %)	pyridinic-N ⁺ -O _x ⁻ (402.7 \pm 0.5 eV) (fractional %)
C ₃ N ₄ - Cu700	32	16.5	57.5	24.5	1.5
C ₃ N ₄ - Cu750	30	64.8	26.9	6.9	1.4
C ₃ N ₄ - Cu800	24	53.7	29.9	15.5	1.0
C ₃ N ₄ - Fe700	9	36.3	21.8	38.6	4.3
C ₃ N ₄ - Fe750	7	45.8	26.1	24.3	3.8
C ₃ N ₄ - Fe800	5	37.8	19.7	40.1	2.5

The C₃N₄-Fe carbons show clear trends of increasing surface area (Figure 5c) and pore volume (Figure 5f,i) with increasing annealing temperature. Although the C₃N₄-Fe700 has the lowest BET surface area of all samples (Figure 5c, orange circles), increasing the annealing temperature to 750 °C and above leads to higher BET surface areas compared to the analogous C₃N₄-Cu carbon (Figure 5c, maroon hexagons and red triangles). In contrast to C₃N₄-Cu carbons, the pore volume (Figure 5f) and pore-size distribution (Figure 5i) of the C₃N₄-Fe carbons show significantly reduced mesoporous character. These differences likely alter the Li⁺ storage mechanism, as the higher specific surface area of the C₃N₄-Fe carbons provides more accessible Li⁺ storage sites, while the larger pore volume in the C₃N₄-Cu creates additional Li⁺ storage sites residing inside pores that minimize the volume changes during cycling compared to Li+ insertion and deinsertion into and out of carbon layers. 25,42,62

The changes in surface chemistry induced by the metal template and annealing temperature were analyzed by XPS (results shown in Figure 6). Comparing the survey scans for bulk C₃N₄ (Figure 6a), C₃N₄-Cu carbons (Figure 6b), and C₃N₄-Fe carbons (Figure 6c) qualitatively shows significant changes in atomic surface composition following metal templating and thermal annealing. The fractional atomic surface composition of the bulk C₃N₄ of 43% C, 56% N, and 1% O (calculated by comparing the compositional areas of deconvoluted high-resolution elemental XPS scans, Figure S6) is consistent with the theoretical composition of C_3N_4 (43% C, 57% N). 25,27,33 A similar analysis of the templated carbons clearly shows a heavy influence of the metal choice on the obtained surface chemistry. The Cu-templated carbons retain an unusually high surface N content of 32% (C₃N₄-Cu700), 30% (C₃N₄-Cu750), and 24% (C₃N₄-Cu800) (additional XPS characterization of C₃N₄-Cu carbons is seen in Figure S7), the highest among the nitrogen-doped carbon anodes designed for LIBs. 21-31,40-48 In contrast, the Fe-templating process significantly reduces the surface nitrogen content to 9%, 7%, and 5% when annealed at 700, 750, and 800 °C, respectively (additional XPS characterization of C₃N₄-Fe carbons is seen in Figure S8). The large change in retained nitrogen content is explained by residual gas analysis (RGA) of the evolved gases during pyrolysis shown in Figure S9. The RGA revealed that Fe templating promotes N2 and CO gas evolution at a significantly lower temperature of 641-647 $^{\circ}\text{C}$ compared to 701-707 °C when Cu is used as the template. The earlier onset of N₂ evolution therefore lowers the resulting nitrogen content of the C₃N₄-Fe carbons at annealing temperatures

above 700 °C (Figure S9). The low residual Cu and Fe content observed by XPS is supported by thermogravimetric analysis (TGA) in air atmosphere to 800 °C of the C_3N_4 -Cu750 and C_3N_4 -Fe750, which revealed a residual mass of only 1.3% and 1.0% for Cu750 and Fe750, respectively.

Not only does the overall nitrogen content differ significantly between C₃N₄-Cu and C₃N₄-Fe, but the relative abundance of the four identified nitrogen functionalities also heavily depends on the metal template (N 1s spectrum of C₃N₄-Cu750 in Figure 6h; N 1s spectrum of C₃N₄-Fe750 in Figure 6i). Comparing the relative abundance of different nitrogen functionalities between the C₃N₄-Cu and C₃N₄-Fe in Table 1 shows that Cu templating favors inclusion of pyridinic-N and pyrrolic-N functionalities, whereas Fe-templating results in comparatively higher fractional graphitic-N and oxidized pyridinic-N groups. Desirably, the 30% surface nitrogen in the C₃N₄-Cu750 carbon is composed of the lowest graphitic-N content (6.9% of overall nitrogen content, which irreversibly reacts with Li⁺) and the highest combined pyridinic-N (64.8% of total surface nitrogen content) and pyrrolic-N (26.9% of total surface N content) that are most favorable for Li+ storage. 21,32

Li⁺ Storage Properties of C₃N₄-Cu and C₃N₄-Fe Nitrogen-Doped Carbons. The Li⁺ electrochemistry of the C₃N₄-derived nitrogen-doped carbons was initially evaluated using cyclic voltammetry (CV) in standard CR2025 coin cells with a Li metal counter/reference electrode (active-material loading: 1.8 ± 0.2 mg cm⁻²; film thickness: $48 \pm 5 \mu$ m supported on 11 μ m thick Cu foil). Figure 7 shows a side-byside comparison of the first three CV cycles (CV curves for bulk C₃N₄ in Figure S11) over the potential range of 0.005-3.0 V (vs Li/Li⁺) for the C₃N₄-Cu (Figure 7a-c, left column with increasing annealing temperature from top to bottom) and C₃N₄-Fe carbons (Figure 7d-f, right column with increasing annealing temperature from top to bottom). The average open-circuit voltage (OCV) for the nitrogen-doped carbons was in the range of 2.6-2.8 V (vs Li/Li⁺), and during the initial discharge (from OCV to 0.005 V; Li⁺ insertion into carbon), all the nitrogen-doped carbons exhibit the following four features: (1) a broad, capacitive-like feature in the range OCV-2.2 V corresponding to faradic reaction of Li⁺ with nitrogen atoms, (2) a feature in the range 1.25-1.0 V corresponding to Li⁺ insertion into pores/defects, (3) a significant feature in the range 0.75-0.5 V corresponding to the irreversible breakdown of the electrolyte on the electrode surface relating to the formation of the solid electrolyte interphase (SEI), and (4) a sharp peak near 0.1 V

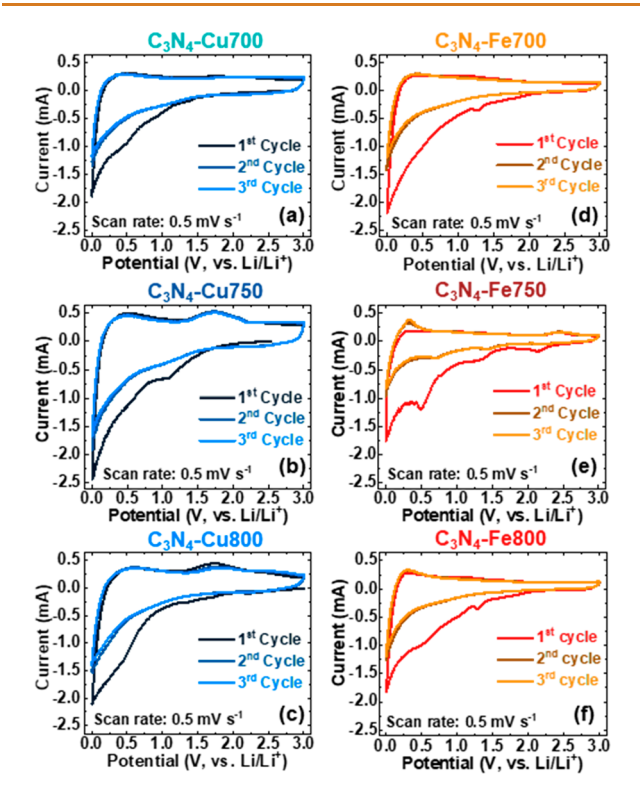


Figure 7. Cyclic voltammetry (CV) curves showing the first three cycles at a scan rate of 0.5 mV s⁻¹ for (a) C_3N_4 -Cu700, (b) C_3N_4 -Cu750, (c) C_3N_4 -Cu800, (d) C_3N_4 -Fe700, (e) C_3N_4 -Fe750, and (f) C_3N_4 -Fe800.

corresponding to the ${\rm Li}^+$ intercalation into carbon layers. $^{22,24,25,28-30,59,61}$ Features (1) and (2) shrink upon subsequent cycling, indicative of the irreversibility of their underlying processes. Following their first cycle forming, the second and third cycle CV traces nearly overlap for all carbons, showing the electrochemical reversibility of the lithiation/delithiation processes.

Although the initial discharge cycle shows similar features regardless of the metal template, the Li⁺ extraction during charging from 0.005 to 3.0 V shows clear evidence of differing Li⁺ storage mechanisms. Li⁺ extraction from C₃N₄-Cu (Figure 7a-c) reveals the following three discernible features: (1) Li⁺ extraction from carbon layers ~0.4 V, (2) Li⁺ extraction from pores and nitrogen defects near 1.6 V, and (3) desorption of Li⁺ from surface N atoms at potentials above 2 V.^{22,24,25,28-30,59,61} The high surface N content and higher relative pore volume of the C₃N₄-Cu show evidence of charge storage contribution via Li+ extraction from pores/defects and pseudocapacitive charge storage through Li-N binding at the electrode surface.²² Comparatively, the lower surface nitrogen content and lower pore volume of the C₃N₄-Fe carbons concurrently restrict the accessible Li⁺ extraction from pores/ defects and show little evidence of meaningful pseudocapacitive charge storage from Li-N binding.

The Li⁺ storage properties of C_3N_4 -Cu and C_3N_4 -Fe were next investigated in galvanostatic charge—discharge tests shown in Figure 8 (charge—discharge analysis of bulk C_3N_4 in Figure S12). The first-cycle charge—discharge curves at 0.05 A g^{-1} for C_3N_4 -Cu (Figure 8a) and C_3N_4 -Fe (Figure 8b) are consistent with the CVs (Figure 7) showing different Li⁺ storage mechanisms for the C_3N_4 -Cu and C_3N_4 -Fe carbons. The charge curves of the C_3N_4 -Cu carbons (Figure 8a) are

angled, sloping lines with only slightly discernible features and notable charge storage contribution throughout the entire 0.005-3.0 V potential window. Of the C₃N₄-Cu carbons, the C₃N₄-Cu700 delivers the lowest initial Coulombic efficiency (CE) of 50% compared to 65% and 63% for C_3N_4 -Cu750 and C₃N₄-Cu800, respectively. In addition to irreversible capacity losses due to SEI formation at the electrode surface, we attribute the lower CE for the C₃N₄-Cu700 carbon to (1) its higher overall and fractional graphitic nitrogen content (see XPS analysis in Figure 6 and Table 1) that will irreversibly react with Li⁺ and (2) its low degree of carbonization that results in higher overpotentials and significantly lower reversible Li⁺ extraction from carbon layers compared to the C₃N₄-Cu750 and C₃N₄-Cu800. Notably, the high pyridinic nitrogen content and large pore volume of the C₃N₄-Cu750 carbon provide the highest initial charge capacity of 988 mAh g^{-1} and the most efficient first cycle at 0.05 A g^{-1} . The Li⁺ extraction features and initial CE of the C_3N_4 -Fe

The Li⁺ extraction features and initial CE of the C_3N_4 -Fe carbons (Figure 8b) show dependence on the degree of graphitization and thus the annealing temperature. The charge curve of the C_3N_4 -Fe700 is like those of the C_3N_4 -Cu carbons and shows the lowest first cycle CE of 49% due to its high graphitic nitrogen content and lack of reversible Li⁺ extraction from graphitic carbon layers (Figure 8b). In contrast, the highly ordered C_3N_4 -Fe750 and C_3N_4 -Fe800 carbons deliver a higher initial CE of 62% and 60%, respectively, owing to their reversible Li⁺ extraction from graphitic carbon layers (evidenced by the plateau near 0.1 V in the charge curves shown in Figure 8b) and the lower probability of irreversible reactions between Li⁺ and surface nitrogen atoms due to their lower overall nitrogen content compared to the C_3N_4 -Fe700 sample. 4,25,29

The rate capability tests of the C_3N_4 -derived carbons at specific currents ranging from 0.1 to 20 A g⁻¹ are displayed in Figure 8c (C_3N_4 -Cu) and Figure 8d (C_3N_4 -Fe). At a low current density of 0.1 A g⁻¹, the average charge capacities of the C_3N_4 -Cu700, C_3N_4 -Cu750, and C_3N_4 -Cu800 were 606, 900, and 648 mAh g⁻¹, respectively. Apparently, the larger pore volume and high pyridinic- and pyrrolic-N content enhance the performance of the C_3N_4 -Cu750 compared to the C_3N_4 -Cu700 and C_3N_4 -Cu800, which lack these characteristics. The C_3N_4 -Cu750 has a uniquely high rate capability (charge—discharge curves in Figure 8e), delivering 572 mAh g⁻¹ at 2 A g⁻¹ (4 mA cm⁻²) and 275 mAh g⁻¹ when charged and discharged in about 1 min at a specific current of 20 A g⁻¹ (40 mA cm⁻²).

Unlike that of C_3N_4 -Cu, the Li⁺ storage capacity of C_3N_4 -Fe at 0.1 A g⁻¹ increases from 482 mAh g⁻¹ at 700 °C to 527 mAh g⁻¹ at 750 °C and 529 mAh g⁻¹ at 800 °C (Figure 8d), less than that of the analogous Cu-templated carbons. Their rate capability is also inferior, dropping below 60 mAh g⁻¹ at 20 A g⁻¹ for all the C_3N_4 -Fe carbons. Considering that the C_3N_4 -Fe have much less N and their total pore volume is lower than those of the C_3N_4 -Cu carbons, it appears that the Li⁺ storage properties of C_3N_4 -derived carbons are defined by their N content and pore volume rather than by their specific surface area.

The differences in performance shown in Figure 8 are well explained by the Figure 9 normalized differential capacity vs voltage (dQ d V^{-1} vs V) plots at 0.1 A g $^{-1}$ (0.2 mA cm $^{-2}$) and 1.0 A g $^{-1}$ (2.0 mA cm $^{-2}$) during the Li $^+$ extraction process (charging). These plots describe the incremental capacity being extracted from the working electrode over a given

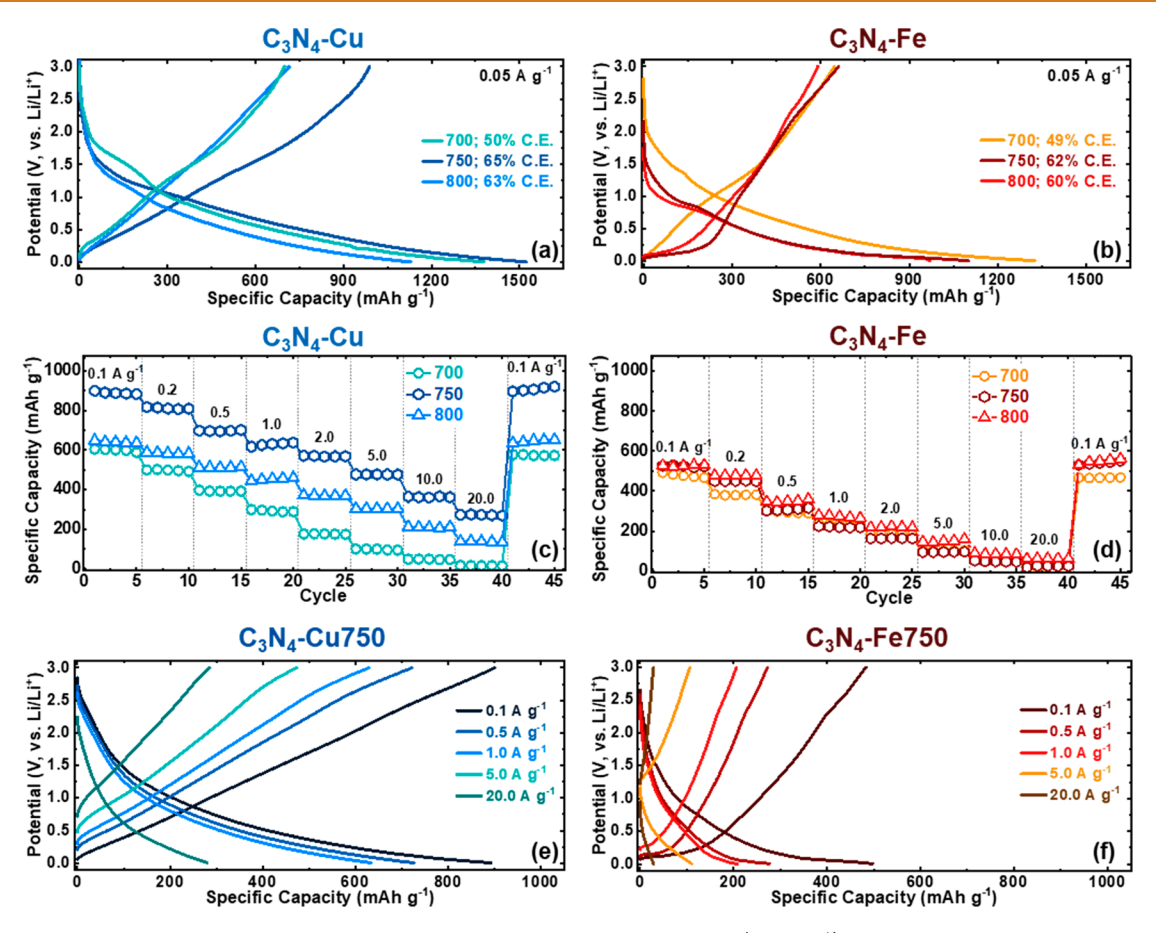


Figure 8. Galvanostatic charge—discharge experiments cycled between 0.005 and 3.0 V (vs Li/Li $^+$) for C₃N4-derived N-doped carbons. (a, b) First-cycle charge—discharge curves of 0.05 A g $^{-1}$ for (a) C₃N₄-Cu and (b) C₃N₄-Fe. (c, d) Rate capability tests from 0.1 to 20 A g $^{-1}$ for (c) C₃N₄-Cu and (d) C₃N₄-Fe. (e, f) Charge—discharge curves at 0.1, 0.5, 1.0, 5.0, and 20 A g $^{-1}$ for (e) C₃N₄-Cu750 and (f) C₃N₄-Fe750.

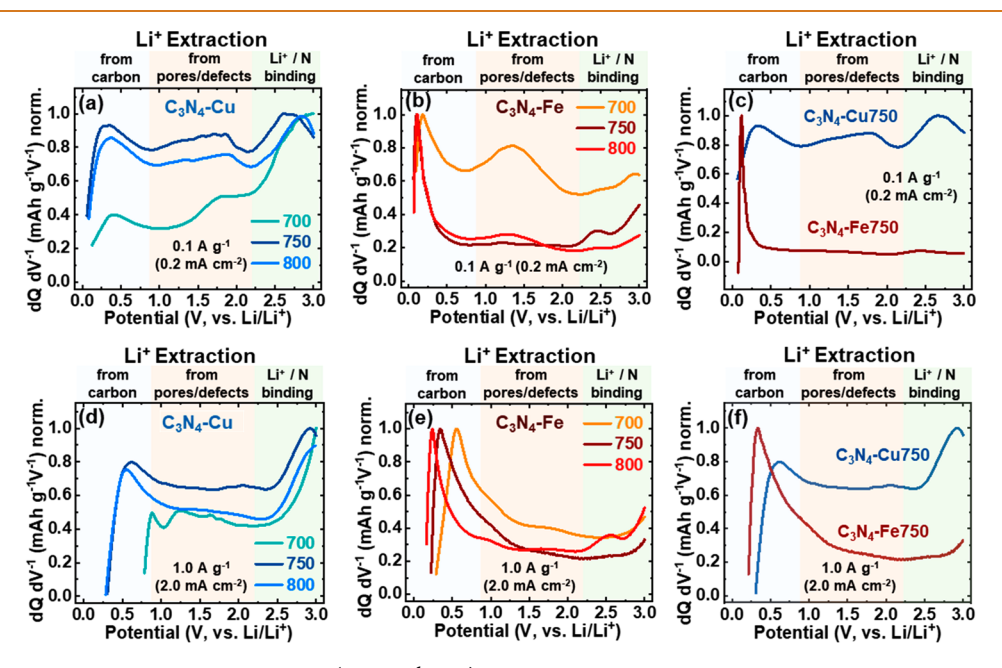


Figure 9. Normalized differential capacity vs voltage (dQ dV⁻¹ vs V) curves of the Li⁺ extraction process in C₃N₄-derived carbons. (a–c, Top row) Normalized dQ dV⁻¹ vs V plots at 0.1 A g⁻¹ (0.2 mA cm⁻²) for (a) C₃N₄-Cu700–800, (b) C₃N₄-Fe700–800, and (c) C₃N₄-Cu750 vs C₃N₄-Fe750. (d–f, Bottom row) Normalized dQ dV⁻¹ vs V plots at 1.0 A g⁻¹ (2.0 mA cm⁻²) for (d) C₃N₄-Cu700–800, (e) C₃N₄-Fe700–800, and (f) C₃N₄-Cu750 vs C₃N₄-Fe750.

voltage range (see the charge–discharge curves from which the $dQ \ dV^{-1} \ \nu s \ V$ plots were constructed in Figures S13 and S14

for C_3N_4 -Cu700–800 and C_3N_4 -Fe700–800, respectively). The dQ dV $^{-1}$ vs V plots at 0.1 A g $^{-1}$ for C_3N_4 -Cu700–800

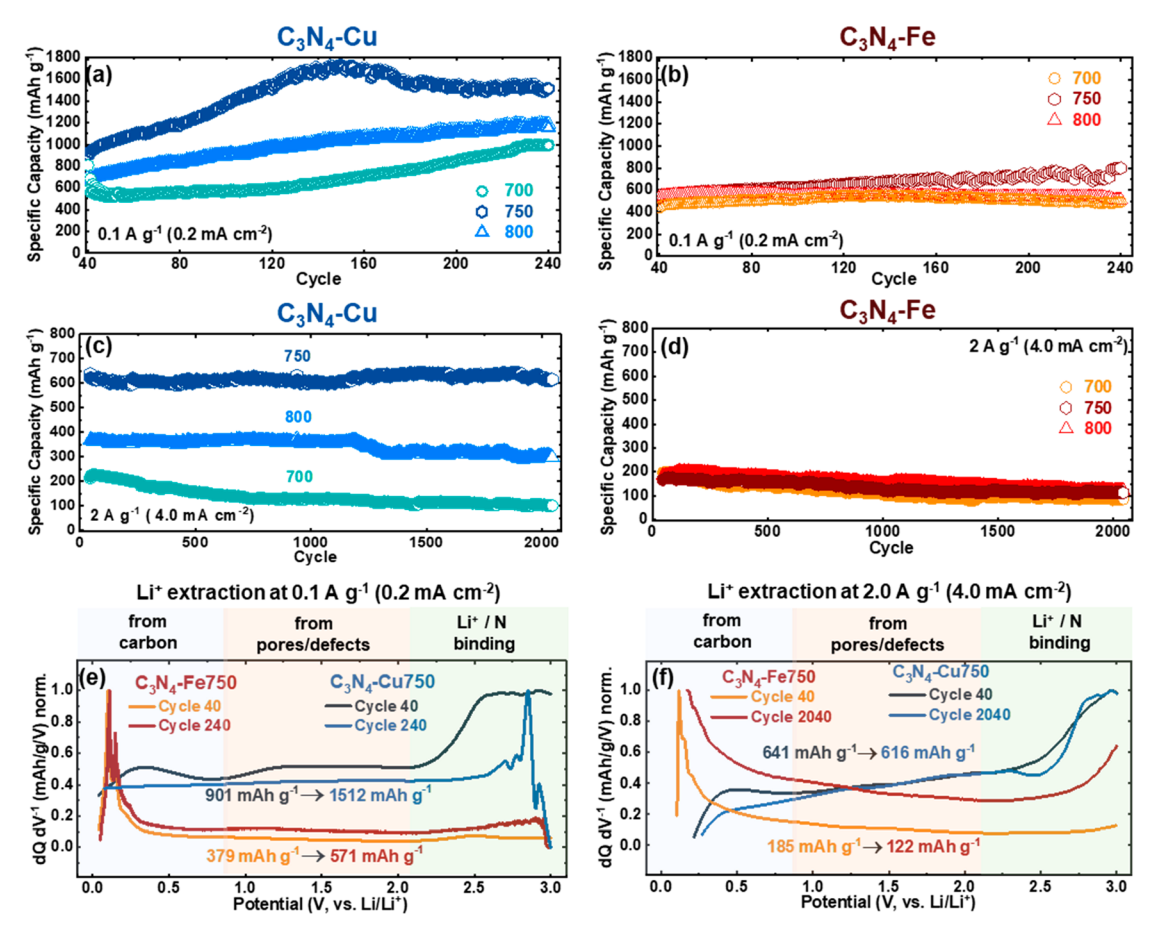


Figure 10. (a, b) Cycling performance over 200 cycles at 0.1 A g^{-1} (following 0.1–20 A g^{-1} cycling as shown in Figure 7c and d) for (a) C_3N_4 -Cu700–800 and (b) C_3N_4 -Fe700–800. (e) Normalized dQ dV⁻¹ vs V plots comparing C_3N_4 -Cu750 (black/navy traces) and C_3N_4 -Fe750 (orange/maroon traces) at cycles 40 and 240. (c, d) Cycling performance over 200 cycles at 2.0 A g^{-1} (following 0.1–20 A g^{-1} cycling as shown in Figure 7c and d) for (c) C_3N_4 -Cu700–800 and (d) C_3N_4 -Fe700–800. (f) Normalized dQ dV⁻¹ vs V plots comparing C_3N_4 -Cu750 (black/navy traces) and C_3N_4 -Fe750 (orange/maroon traces) at cycles 40 and 2040.

(Figure 9a, top left) show significant capacity contribution throughout the entire potential window (0.005–3.0 V vs Li/Li⁺), attributed to extraction of Li⁺ from (1) carbon layers (0.005–0.8 V; light purple region), (2) pores and defects (~1.0–2.2 V; salmon region), and (3) Li⁺ binding to heteroatoms at the electrode surface (~2.2–3.0 V; light green region). ^{22,25,50,62} In contrast, only the C₃N₄-Fe700 (Figure 9b, orange trace) shows contributions from both carbon layers (at ~0.25–0.3 V) and pores/defects at ~1.25 V, while the capacity is largely a result of Li⁺ extraction from carbon layers in the more ordered C₃N₄-Fe750 (Figure 9b, maroon trace) and C₃N₄-Fe800 (Figure 9b, red trace).

When the charge—discharge current is increased to 1.0 A g^{-1} (2.0 mA cm⁻²), the relative contributions from the different Li⁺ extraction processes change for both C_3N_4 -Cu700—800 (Figure 9d) and C_3N_4 -Fe700—800 (Figure 9e). The higher overpotential (notice the shift in the starting potential on the *x*-axis; see Figure S15 for further dQ dV⁻¹ vs V analysis) at the higher current density restricts the efficiency of Li⁺ extraction from carbon layers that occurs at lower potential than extraction from pores/defects and Li⁺ binding to N atoms. This is evidenced by the lower relative contribution in this region for C_3N_4 -Cu (Figure 9d) and the broadening of the Li⁺ extraction feature for C_3N_4 -Fe (Figure 9e). The higher overpotential and limited capacity contribution from pores/defects and Li–N binding therefore restrict the rate capability

of C₃N₄-Fe (Figure 8d). In contrast, the higher N content and larger pore volume compensate for the losses in Li⁺ extraction from carbon layers at higher overpotential and endow C₃N₄-Cu with higher rate capability. It is noteworthy that the relative contribution from surface Li–N binding increases at higher current density, highlighting the benefit of high N content for enhancing the diffusion-independent, pseudocapacitive storage from surface Li⁺ binding (Figure 9f). This assertion is supported by variable scan-rate CV analysis (see page S-16) of C₃N₄-Cu700–800 and C₃N₄-Fe700–800 shown in Figure S16 and Figure S17, respectively. The "b-value" analysis (page S-18 and eq S1) at different scan rates deconvolutes the underlying mass-transport character of the Li⁺ extraction mechanism and shows a higher capacitive contribution to the overall charge storage of C₃N₄-Cu due to the much higher N

Following rate capability tests from 0.1 to 20 A $\rm g^{-1}$ (Figure 8c,d), the cycle stability of the $\rm C_3N_4$ -derived carbon was tested at both 0.1 A $\rm g^{-1}$ (Figure 10a,b) and 2 A $\rm g^{-1}$ (Figure 10c,d) for $\rm C_3N_4$ -Cu700–800 (Figure 9a,c) and $\rm C_3N_4$ -Fe700–800 (Figure 9b,d). At a low current density of 0.1 A $\rm g^{-1}$, all the $\rm C_3N_4$ -derived carbons showed a gradual increase in capacity with cycle progression over 200 cycles that can be attributed to increased activation of pores and defects with increased cycling and electrolyte penetration into the depth of the porous active materials. 23,25,30 The larger capacity enhancement for $\rm C_3N_4$ -Cu

(see charge—discharge curves at different cycle number and corresponding Coulombic efficiency plots in Figure S18 for C_3N_4 -Cu700—800 and Figure S19 for C_3N_4 -Fe700—800) is attributed to their larger active pore size that increases with the cycle number. Most notably, for C_3N_4 -Cu750 the charge capacity increases to a maximum of 1720 mAh g⁻¹ at cycle 150 and stabilizes at around 1500 mAh g⁻¹ at cycle 240 (Figure 10a). The capacity enhancement appears rooted in the activation of pore defects and an associated increase in activity in Li–N binding, as evidenced by the emergence of well-defined peaks in the range of 2.5–3.0 V in the dQ dV⁻¹ vs V plot at cycle 240 for C_3N_4 -Cu750 (Figure 10e, navy trace) that are absent in the C_3N_4 -Fe750 curves (Figure 10e, maroon and orange traces).

At the higher specific current of 2 A g^{-1} (~4 mA cm⁻²), the cycle stability of the C₃N₄-derived carbons differs significantly over 2000 cycles. While C₃N₄-Cu750 has an excellent capacity retention of 96% over 2000 cycles (dropping from 641 mAh g^{-1} at cycle 40 to 616 mAh g^{-1} at cycle 2040, Figure 10c), the capacity retention drops to merely 47% for C₃N₄-Cu700 and to 80% for C₃N₄-Cu800 after 2000 cycles (see chargedischarge curves and Coulombic efficiency plots for C₃N₄-Cu700-800 in Figure S20). On the other hand, the C_3N_4 -Fe carbons (Figure 10d) all show significant capacity loss over 2000 cycles at 2 A g⁻¹, retaining only 44%, 65%, and 67% at 700, 750, and 800 °C, respectively (see charge–discharge curves and Coulombic efficiency plots for C₃N₄-Fe700-800 in Figure S21). These trends are explained by the dQ dV^{-1} vs V curves at cycle 40 and cycle 2040 for C₃N₄-Cu750 (black/navy traces) and C₃N₄-Fe750 (maroon/orange traces) in Figure 10f. After 2000 cycles at 2 A g⁻¹, the C₃N₄-Fe750 carbon shows a reduction in Li+ extraction capacity from carbon layers (compare orange and maroon curves in Figure 10f) that limits the achievable capacity at faster current density. The C_3N_4 -Cu750 carbon shows evidence of highly reversible and stable Li+ extraction from pores/defects and Li-N surface binding that enables excellent capacity retention over 2000 cycles (Figure 10f, black and navy traces) that is largely absent in the C_3N_4 -Fe750 dQ dV $^{-1}$ vs V curves.

The utility of the highest performing C₃N₄-Cu750 carbon as a high-capacity LIB anode was further evaluated by increasing the mass loading from 1.8-2.0 mg cm⁻² (as discussed above) to 3.0-3.2 and 4.4-4.6 mg cm⁻² (Figure 11a). As the loading was increased to \sim 3.1 and 4.5 mg cm⁻², the specific capacity at 0.1 A g^{-1} was reduced from 900 mAh g^{-1} (at 1.8-2.0 mgcm⁻²) to 630 and 580 mAh g⁻¹, respectively (Figure S22). Despite the drop in specific capacity, the fabrication of higher loading electrode films resulted in a higher areal capacity normalized to the geometric electrode area (0.97 cm²; Figure 11a). The C₃N₄-Cu750 loaded with 4.5 mg cm⁻² delivered the highest areal capacity of 2.6 mAh cm^{-2} at 0.1 A g^{-1} (0.45 mA cm^{-2}) and still delivered 0.2 mAh cm^{-2} at 20 Å g^{-1} (90 mA cm⁻²). These metrics compare favorably with those of earlier high-performance carbon LIB anodes as shown in Figure 11b. To account for differences in active-material loading, the C₃N₄-Cu750 performance is compared only with other carbons for which active-material loadings have been provided.^{20,24,40-48} Table S3 in the Supporting Information lists the information underlying data used to construct Figure 11b, and while most reports of high-performance carbon anodes for LIBs report specific capacities exceeding 1000 mAh g⁻¹ at low current density, their active-material loadings are often below 1 mg cm⁻². Their low active-material loading would not match the

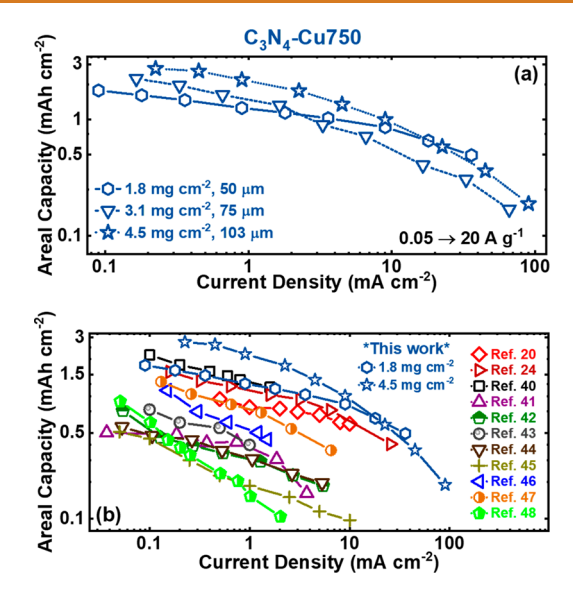


Figure 11. (a) Areal rate capability (between 0.1 and 20 A g $^{-1}$) of $C_3N_4\text{-}\text{Cu}750$ at mass loadings of 1.8 mg cm $^{-2}$ (hexagons), 3.1 mg cm $^{-2}$ (downward triangles), and 4.5 mg cm $^{-2}$ (stars). (b) Comparison of the areal rate capability of $C_3N_4\text{-}\text{Cu}750$ at 1.8 mg cm $^{-2}$ (navy hexagons) and 4.5 mg cm $^{-2}$ (navy stars) to other reported high-capacity carbon anode materials. Please note that, to account for variation between mass loading in different studies, we only compare here those reports that provided active-material loadings in their report.

cathode capacity of commercial LIB cathode loadings providing 2.5–3.0 mAh cm $^{-2}$, and we therefore compare the areal capacities of the reported carbon materials. 3,10 The moderate specific surface of $\rm C_3N_4\text{-}Cu750$, 391 m 2 g $^{-1}$ compared to >600 m 2 g $^{-1}$ of most studies, allows for the fabrication of higher mass loading electrodes without mechanical degradation, and the large pore volume (1.527 cm 3 g $^{-1}$) and high nitrogen content (30%) contribute significant capacitive-like charge storage that endows $\rm C_3N_4\text{-}Cu750$ with high capacity and rate capability.

CONCLUSION

In summary, Cu templating transforms pristine C₃N₄ into nitrogen-doped carbons of potential utility as LIB anodes. The favorable surface chemistry, textural properties, and resulting Li⁺ storage performance of the nitrogen-doped carbons are a consequence of the extent of metal alloying with carbon and nitrogen. Unlike the alloying Fe that produces carbons with a high degree of graphitization, low nitrogen content (<10%), and moderate pore volume, the carbons formed with the nonalloying Cu are highly defective with a high nitrogen content (32–24%) and a larger pore volume. Cu templating is beneficial to Li⁺ storage, with the carbon formed at 750 °C delivering the highest specific capacity of 900 mAh g⁻¹ at 0.1 A g⁻¹ and 275 mAh g⁻¹ at 20 A g⁻¹, while also retaining 96% of its initial capacity after 2000 cycles at 2 A g⁻¹. The fabrication of higher mass loading electrodes (4.5 mg cm⁻²) provided a maximum areal capacity of 2.6 mAh cm⁻² at 0.45 mA cm⁻² (0.1 A g⁻¹), comparable to the capacities of commercial LIB cells and favorable compared to other reported carbon materials.

METHODS

Synthesis of C₃N₄-Cu and C₃N₄-Fe Nitrogen-Doped Car**bons.** C₃N₄-Cu and C₃N₄-Fe were prepared by a templating/thermal annealing method as shown in Figure 1. The bulk C₃N₄ was first synthesized by the conventional thermal condensation of urea at 550 °C.³³ Typically, urea (99%, Sigma-Aldrich) was placed in a covered crucible and ramped from ambient temperature at 2.3 °C min⁻¹ to 550 °C for 4 h in static air. The bulk C₃N₄ was then manually mixed in a 1:1 (w/w) ratio with either Cu powder (99.7%, Sigma Aldrich; "C₃N₄-Cu") or Fe powder (99.9%, Sigma-Aldrich; "C₃N₄-Fe") using a mortar and pestle for 15 min. The mixed powders were placed in a covered crucible and ramped from ambient temperature to 700 °C $(C_3N_4$ -Cu700 or C_3N_4 -Fe700), 750 °C $(C_3N_4$ -Cu750 or C_3N_4 -Fe750), or 800 °C (C_3N_4 -Cu800 or C_3N_4 -Fe800) at 10 °C min⁻¹ held for 2 h at each respective temperature. The recovered products were then washed by slow addition of concentrated HNO3 when Cu was used as the template and HCl when Fe was used as the template. **CAUTION:** The reaction between Cu and HNO₃ liberates toxic NO₂(g), and the reaction between Fe and HCl produces flammable $H_2(g)$. Therefore, care must be taken during the slow addition of HNO3 and HCl, and all washing procedures should be conducted in a well-ventilated fume hood. After slight stirring at ambient temperature for 20 min, the acid baths were diluted with excess DI H2O and filtered. After repeating this process three times, the resultant black powders were washed with excess DI water and ethanol and dried at 60 °C under vacuum for 12 h to afford the C₃N₄-Cu and C₃N₄-Fe carbons.

Characterization. SEM images of the bulk C₃N₄, C₃N₄-Cu, and C₃N₄-Fe were collected on a Hitachi S5500 SEM/STEM. The samples were prepared via drop-casting the respective materials onto a Si wafer from a dilute ethanol suspension. For transmission electron microscopy (TEM) a JEOL 2010F transmission electron microscope was used. X-ray diffraction patterns were recorded on a Rigaku Miniflex 600 diffractometer using monochromatic Cu K α radiation (λ = 1.5418 Å). X-ray patterns were measured in the 5–70° 2θ range in a continuous scan mode (1° min⁻¹) with a step width of $2\theta = 0.025^{\circ}$. Raman spectra were recorded on a Renishaw inVia Raman microscope with a 532 nm (2.33 eV, green) laser operated at 70 mW. Nitrogen adsorption-desorption isotherms at 77 K were collected using a Quantachrome Nova2200e volumetric gas sorption analyzer. The specific surface areas of the samples were derived using BET theory, and their pore-size distributions were derived using QSDFT (slit-pore on carbon). XPS was conducted on a Kratos Axis Ultra DLD X-ray photoelectron spectrometer with a depth resolution of 2 to 8 nm and a detection limit of 0.1 to 1.0 at. %. TGA was performed on a Mettler thermogravimetric analyzer, model TGA/ DSC 1, under air atmosphere with a ramp rate of 10 $^{\circ}\text{C}$ min $^{-1}$ from room temperature to 800 °C. RGA was performed on the effluent stream during annealing. In a typical experiment, 550 mg of a 1:1 (w/ w) mixture of either C₃N₄/Cu or C₃N₄/Fe was supported on a quartz wool plug in a vertically aligned quartz tube and held inside an Applied Test Systems model 3210 tube furnace. MKS type M100B mass flow controllers were used to deliver Ar to the sample bed. The effluent was monitored using a custom-built gas analysis system consisting of an Extorr XT100 residual gas analyzer operating in a stainless-steel chamber with a base operating pressure of 5 \times 10^{-10} Torr. Effluent gas was introduced to the analysis chamber at a pressure of 1.0×10^{-6} Torr through a temperature-controlled leak

Electrochemical Measurements. The bulk C_3N_4 , C_3N_4 -Cu, and C_3N_4 -Fe electrode films were prepared by mixing the active material with carbon black (Super P, MTI Corporation) and poly(vinylidene difluoride) (MTI Corporation) in a 8:1:1 ratio using N-methyl-2-pyrrolidone (Sigma-Aldrich) as solvent. The slurries were coated onto Cu foil (11 μ m thick, MTI Corporation) using an automatic film coater with an adjustable doctor blade gap (50–250 μ m; MTI Corporation) and subsequently dried under vacuum at 120 °C for 16 h. The dried electrodes were then slightly pressed using a calender (MRX-SG100L, Polaris Battery Laboratories) and punched into individual electrodes (0.97 cm²). The weight of the individual

electrodes was recorded on a Mettler Toledo XS225DU Semi-Micro balance with a readability of 0.01 mg, and the thickness of the electrodes was measured using a digital micrometer with $\pm 1~\mu m$ resolution (Mitutoyo 293 series). The electrodes were assembled into standard CR2032 coin cells with Li foil (Alfa Aesar, 99.9%) as the counter/reference electrode, a Celgard 2400 polypropylene separator, and 150 µL of 1.2 M LiPF₆ in 3:7 ethylene carbon/dimethyl carbonate (v/v) as electrolyte. Prior to all electrochemical testing the cells were kept at OCV for 12 h. CV and galvanostatic chargedischarge (GCD) tests were conducted on a 40-channel battery analyzer (LBT2000, Arbin). The CV tests were conducted between 0.005 and 3.0 V (vs Li/Li+) for three cycles at each of the following scan rates: 0.5, 1.0, 2.0, 5.0, and 10.0 mV s⁻¹. The GCD tests were conducted over the same potential range as in the CV experiments, and each cell was first cycled at 0.05 Å g⁻¹ (based on the mass of active material on the electrode) for three cycles to form the SEI layer and begin activation of the active materials. The rate capability tests were conducted at 0.1, 0.2, 0.5, 1.0, 2.0, 5.0, 10.0, and 20.0 A g⁻¹ for 5 cycles at each respective applied charge-discharge current. Electrochemical impedance spectroscopy (EIS) analysis was performed using a Gamry Interface 1010E potentiostat in the frequency range of 0.01-100 000 Hz with an amplitude of 5 mV.

ASSOCIATED CONTENT

S Supporting Information

The Supporting Information is available free of charge on the ACS Publications website at DOI: 10.1021/acsnano.9b03861.

Additional SEM characterization of bulk C_3N_4 , C_3N_4 -Cu, and C_3N_4 -Fe; Raman fitting for C_3N_4 -Cu and C_3N_4 -Fe; deconvoluted high-resolution C 1s and N 1s XPS spectra of bulk C_3N_4 , C_3N_4 -Cu, and C_3N_4 -Fe; CV and GCD analysis of bulk C_3N_4 ; charge—discharge plots for C_3N_4 -Cu and C_3N_4 -Fe carbons at various charge—discharge rates and over long-term cycling; variable scanrate CV analysis of C_3N_4 -Cu and C_3N_4 -Fe; specific capacity at different current density for C_3N_4 -Cu750 at different mass loading; table listing the parameters obtained from other reports to construct Figure 10b; EIS analysis of bulk C_3N_4 , C_3N_4 -Cu, and C_3N_4 -Fe (PDF)

AUTHOR INFORMATION

Corresponding Author

*E-mail: mullins@che.utexas.edu.

ORCID

Joshua P. Pender: 0000-0002-2231-8373 Joseph V. Guerrera: 0000-0003-1088-4535 Jason A. Weeks: 0000-0003-0335-6128 Ryan A. Ciufo: 0000-0001-9192-9832 James N. Burrow: 0000-0002-7445-3788 Mohammad Z. Rahman: 0000-0003-3264-4778

Adam Heller: 0000-0003-0181-1246 C. Buddie Mullins: 0000-0003-1030-4801

Notes

The authors declare no competing financial interest.

ACKNOWLEDGMENTS

The authors gratefully acknowledge the generous and continued support of the Welch Foundation through grants F-1131 (A.H.) and F-1436 (C.B.M.) as well as the National Science Foundation *via* grant no. CBET-1603491. The authors also thank Celgard for generously providing membrane separators.

REFERENCES

- (1) Goodenough, J. B.; Park, K.-S. S. The Li-Ion Rechargeable Battery: A Perspective. J. Am. Chem. Soc. 2013, 135, 1167–1176.
- (2) Blomgren, G. E. The Development and Future of Lithium Ion Batteries. *J. Electrochem. Soc.* **2017**, *164*, 5019–5025.
- (3) Andre, D.; Hain, H.; Lamp, P.; Maglia, F.; Stiaszny, B. Future High-Energy Density Anode Materials from an Automotive Application Perspective. J. Mater. Chem. A 2017, 5, 17174–17198.
- (4) Andre, D.; Kim, S.-J.; Lamp, P.; Lux, S. F.; Maglia, F.; Paschos, O.; Stiaszny, B. Future Generations of Cathode Materials: An Automotive Industry Perspective. *J. Mater. Chem. A* **2015**, *3*, 6709–6732.
- (5) Armand, M.; Tarascon, J.-M. Building Better Batteries. *Nature* 2008, 451, 652-657.
- (6) Sun, Y.-K.; Chen, Z.; Noh, H.-J.; Lee, D.-J.; Jung, H.-G.; Ren, Y.; Wang, S.; Yoon, C. S.; Myung, S.-T.; Amine, K. Nanostructured High-Energy Cathode Materials for Advanced Lithium Batteries. *Nat. Mater.* **2012**, *11*, 942–947.
- (7) Myung, S. T.; Maglia, F.; Park, K. J.; Yoon, C. S.; Lamp, P.; Kim, S. J.; Sun, Y. K. Nickel-Rich Layered Cathode Materials for Automotive Lithium-Ion Batteries: Achievements and Perspectives. *ACS Energy Lett.* **2017**, *2*, 196–223.
- (8) Schipper, F.; Erickson, E. M.; Erk, C.; Shin, J.-Y.; Chesneau, F. F.; Aurbach, D. Recent Advances and Remaining Challenges for Lithium Ion Battery Cathodes. *J. Electrochem. Soc.* **2017**, *164*, A6220—A6228.
- (9) Nitta, N.; Yushin, G. High-Capacity Anode Materials for Lithium-Ion Batteries: Choice of Elements and Structures for Active Particles. *Part. Part. Syst. Charact.* **2014**, *31*, 317–336.
- (10) Gallagher, K. G.; Trask, S. E.; Bauer, C.; Woehrle, T.; Lux, S. F.; Tschech, M.; Lamp, P.; Polzin, B. J.; Ha, S.; Long, B.; Wu, Q.; Lu, W.; Dees, D. W.; Jansen, A. N. Optimizing Areal Capacities through Understanding the Limitations of Lithium-Ion Electrodes. *J. Electrochem. Soc.* **2016**, *163*, A138—A149.
- (11) Wood, D. L.; Li, J.; Daniel, C. Prospects for Reducing the Processing Cost of Lithium Ion Batteries. *J. Power Sources* **2015**, 275, 234–242.
- (12) Xiao, H.; Pender, J. P.; Meece-Rayle, M. A.; De Souza, J. P.; Klavetter, K. C.; Ha, H.; Lin, J.; Heller, A.; Ellison, C. J.; Mullins, C. B. Reduced-Graphene Oxide/Poly(Acrylic Acid) Aerogels as a Three-Dimensional Replacement for Metal-Foil Current Collectors in Lithium-Ion Batteries. ACS Appl. Mater. Interfaces 2017, 9, 22641—22651.
- (13) Pender, J. P.; Xiao, H.; Dong, Z.; Cavallaro, K. A.; Weeks, J. A.; Heller, A.; Ellison, C. J.; Mullins, C. B. Compact Lithium-Ion Battery Electrodes with Lightweight Reduced Graphene Oxide/Poly(Acrylic Acid) Current Collectors. *ACS Appl. Energy Mater.* **2019**, *2*, 905–912.
- (14) Lee, J. H.; Yoon, C. S.; Hwang, J.-Y.; Kim, S.-J.; Maglia, F.; Lamp, P.; Myung, S.-T.; Sun, Y.-K. High-Energy-Density Lithium-Ion Battery Using a Carbon-Nanotube—Si Composite Anode and a Compositionally-Graded Li[Ni_{0.85}Co_{0.05}Mn_{0.10}]O₂ Cathode. *Energy Environ. Sci.* **2016**, *9*, 2152–2158.
- (15) Yu, S. H.; Lee, S. H.; Lee, D. J.; Sung, Y. E.; Hyeon, T. Conversion Reaction-Based Oxide Nanomaterials for Lithium Ion Battery Anodes. *Small* **2016**, *12*, 2146–2172.
- (16) Cabana, J.; Monconduit, L.; Larcher, D.; Palacín, M. R. Beyond Intercalation-Based Li-Ion Batteries: The State of the Art and Challenges of Electrode Materials Reacting through Conversion Reactions. *Adv. Mater.* **2010**, 22, 170–192.
- (17) Wu, F.; Yushin, G. Conversion Cathodes for Rechargeable Lithium and Lithium-Ion Batteries. *Energy Environ. Sci.* **2017**, *10*, 435–459.
- (18) Goriparti, S.; Miele, E.; De Angelis, F.; Di Fabrizio, E.; Proietti Zaccaria, R.; Capiglia, C. Review on Recent Progress of Nanostructured Anode Materials for Li-Ion Batteries. *J. Power Sources* **2014**, 257, 421–443.
- (19) Wang, Y.; Wang, Z.; Yu, X.; Li, B.; Kang, F.; He, Y.-B. Hierarchically Structured Carbon Nanomaterials for Electrochemical Energy Storage Applications. *J. Mater. Res.* **2018**, 33, 1058–1073.

(20) Kaskhedikar, N. A.; Maier, J. Lithium Storage in Carbon Nanostructures. *Adv. Mater.* **2009**, *21*, 2664–2680.

- (21) Ma, C.; Shao, X.; Cao, D. Nitrogen-Doped Graphene Nanosheets as Anode Materials for Lithium Ion Batteries: A First-Principles Study. *J. Mater. Chem.* **2012**, 22, 8911–8915.
- (22) Ma, C.; Deng, C.; Liao, X.; He, Y.; Ma, Z.; Xiong, H. Nitrogen and Phosphorus Codoped Porous Carbon Framework as Anode Material for High Rate Lithium-Ion Batteries. *ACS Appl. Mater. Interfaces* **2018**, *10*, 36969–36975.
- (23) Dong, J.; Xue, Y.; Zhang, C.; Weng, Q.; Dai, P.; Yang, Y.; Zhou, M.; Li, C.; Cui, Q.; Kang, X.; Tang, C.; Bando, Y.; Golberg, D.; Wang, X. Improved Li⁺ Storage through Homogeneous *N*-Doping within Highly Branched Tubular Graphitic Foam. *Adv. Mater.* **2017**, *29*, 1–8.
- (24) Li, J.; Zhang, F.; Wang, C.; Shao, C.; Li, B.; Li, Y.; Wu, Q.-H.; Yang, Y. Self Nitrogen-Doped Carbon Nanotubes as Anode Materials for High Capacity and Cycling Stability Lithium-Ion Batteries. *Mater. Des.* 2017, 133, 169–175.
- (25) Chen, J.; Mao, Z.; Zhang, L.; Wang, D.; Xu, R.; Bie, L.; Fahlman, B. D. Nitrogen-Deficient Graphitic Carbon Nitride with Enhanced Performance for Lithium Ion Battery Anodes. *ACS Nano* **2017**, *11*, 12650–12657.
- (26) Zhang, H.; Yang, J.; Hou, H.; Chen, S.; Yao, H. Nitrogen-Doped Carbon Paper with 3D Porous Structure as a Flexible Free-Standing Anode for Lithium-Ion Batteries. *Sci. Rep.* **2017**, *7*, 1–9.
- (27) Pan, H. Graphitic Carbon Nitride Nanotubes As Li-Ion Battery Materials: A First-Principles Study. *J. Phys. Chem. C* **2014**, *118*, 9318–9323.
- (28) Tian, L. L.; Wei, X. Y.; Zhuang, Q. C.; Jiang, C. H.; Wu, C.; Ma, G. Y.; Zhao, X.; Zong, Z. M.; Sun, S. G. Bottom-up Synthesis of Nitrogen-Doped Graphene Sheets for Ultrafast Lithium Storage. *Nanoscale* **2014**, *6*, 6075–6083.
- (29) Liu, C.; Liu, X.; Tan, J.; Wang, Q.; Wen, H.; Zhang, C. Nitrogen-Doped Graphene by All-Solid-State Ball-Milling Graphite with Urea as a High-Power Lithium Ion Battery Anode. *J. Power Sources* **2017**, 342, 157–164.
- (30) Huang, S.; Li, Z.; Wang, B.; Zhang, J.; Peng, Z.; Qi, R.; Wang, J.; Zhao, Y. N-Doping and Defective Nanographitic Domain Coupled Hard Carbon Nanoshells for High Performance Lithium/Sodium Storage. *Adv. Funct. Mater.* **2018**, 28, 1–10.
- (31) Liu, X.; Zhang, J.; Guo, S.; Pinna, N. Graphene/N-Doped Carbon Sandwiched Nanosheets with Ultrahigh Nitrogen Doping for Boosting Lithium-Ion Batteries. *J. Mater. Chem. A* **2016**, *4*, 1423–1431
- (32) Veith, G. M.; Baggetto, L.; Adamczyk, L. A.; Guo, B.; Brown, S. S.; Sun, X. G.; Albert, A. A.; Humble, J. R.; Barnes, C. E.; Bojdys, M. J.; Dai, S.; Dudney, N. J. Electrochemical and Solid-State Lithiation of Graphitic C₃N₄. *Chem. Mater.* **2013**, *25*, 503–508.
- (33) Kessler, F. K.; Zheng, Y.; Schwarz, D.; Merschjann, C.; Schnick, W.; Wang, X.; Bojdys, M. J. Functional Carbon Nitride Materials-Design Strategies for Electrochemical Devices. *Nat. Rev. Mater.* **2017**, 2, DOI: 10.1038/natreymats.2017.30
- (34) Matsoso, B. J.; Ranganathan, K.; Mutuma, B. K.; Lerotholi, T.; Jones, G.; Coville, N. J. Time-Dependent Evolution of the Nitrogen Configurations in *N*-Doped Graphene Films. *RSC Adv.* **2016**, *6*, 106914–106920.
- (35) Stoyanov, S. R.; Titov, A. V.; Král, P. Transition Metal and Nitrogen Doped Carbon Nanostructures. *Coord. Chem. Rev.* **2009**, 253, 2852–2871.
- (36) Babu, D. J.; Bruns, M.; Schneider, R.; Gerthsen, D.; Schneider, J. J. Understanding the Influence of N-Doping on the CO_2 Adsorption Characteristics in Carbon Nanomaterials. J. Phys. Chem. C **2017**, 121, 616–626.
- (37) Jiang, L.; Yuan, X.; Pan, Y.; Liang, J.; Zeng, G.; Wu, Z.; Wang, H. Doping of Graphitic Carbon Nitride for Photocatalysis: A Review. *Appl. Catal., B* **2017**, *217*, 388–406.
- (38) Leela, A.; Reddy, M.; Srivastava, A.; Gowda, S. R.; Gullapalli, H.; Dubey, M.; Ajayan, P. M. Synthesis Of Nitrogen-Doped Graphene Films For Lithium Battery Application. *ACS Nano* **2010**, *4*, 6337–6342.

(39) Liu, Y.; Huang, L.; Wei, D.; Wang, Y.; Zhang, H.; Yu, G. Synthesis of *N*-Doped Graphene by Chemical Vapor Deposition and Its Electrical Properties. *Nano Lett.* **2009**, *9*, 1752–1758.

- (40) Ewels, C. P.; Glerup, M. Nitrogen Doping in Carbon Nanotubes. J. Nanosci. Nanotechnol. 2005, 5, 1345–1363.
- (41) Jansen, R. J. J.; van Bekkum, H. XPS of Nitrogen-Containing Functional Groups on Activated Carbon. *Carbon* **1995**, 33, 1021–1027.
- (42) Zheng, F.; Yang, Y.; Chen, Q. High Lithium Anodic Performance of Highly Nitrogen-Doped Porous Carbon Prepared from a Metal-Organic Framework. *Nat. Commun.* **2014**, *5*, 1–10.
- (43) Zhou, X.; Čhen, F.; Bai, T.; Long, B.; Liao, Q.; Ren, Y.; Yang, J. Interconnected Highly Graphitic Carbon Nanosheets Derived from Wheat Stalk as High Performance Anode Materials for Lithium Ion Batteries. *Green Chem.* **2016**, *18*, 2078–2088.
- (44) Zhu, S.; Li, J.; Ma, L.; Guo, L.; Li, Q.; He, C.; Liu, E.; He, F.; Shi, C.; Zhao, N. Three-Dimensional Network of N-Doped Carbon Ultrathin Nanosheets with Closely Packed Mesopores: Controllable Synthesis and Application in Electrochemical Energy Storage. ACS Appl. Mater. Interfaces 2016, 8, 11720–11728.
- (45) Zhang, J.; Zhu, H.; Wu, P.; Ge, C.; Sun, D.; Xu, L.; Tang, Y.; Zhou, Y. Rational Synthesis of Ni Nanoparticle-Embedded Porous Graphitic Carbon Nanosheets with Enhanced Lithium Storage Properties. *Nanoscale* **2015**, *7*, 18211–18217.
- (46) Song, H.; Yang, G.; Wang, C. General Scalable Strategy Toward Heterogeneously Doped Hierarchical Porous Graphitic Carbon Bubbles for Lithium-Ion Battery Anodes. *ACS Appl. Mater. Interfaces* **2014**, *6*, 21661–21668.
- (47) Lyu, Z.; Yang, L.; Xu, D.; Zhao, J.; Lai, H.; Jiang, Y.; Wu, Q.; Li, Y.; Wang, X.; Hu, Z. Hierarchical Carbon Nanocages as High-Rate Anodes for Li- and Na-Ion Batteries. *Nano Res.* **2015**, *8*, 3535–3543. (48) Gaddam, R. R.; Yang, D.; Narayan, R.; Raju, K. V. S. N.;
- Kumar, N. A.; Zhao, X. S. Biomass Derived Carbon Nanoparticle as Anodes for High Performance Sodium and Lithium Ion Batteries. *Nano Energy* **2016**, *26*, 346–352.
- (49) Ouyang, H.; Gong, Q.; Li, C.; Huang, J.; Xu, Z. Porphyra Derived Hierarchical Porous Carbon with High Graphitization for Ultra-Stable Lithium-Ion Batteries. *Mater. Lett.* **2019**, 235, 111–115.
- (50) Li, Z.; Xu, Z.; Tan, X.; Wang, H.; Holt, C. M. B.; Stephenson, T.; Olsen, B. C.; Mitlin, D. Mesoporous Nitrogen-Rich Carbons Derived from Protein for Ultra-High Capacity Battery Anodes and Supercapacitors. *Energy Environ. Sci.* **2013**, *6*, 871–878.
- (\$1) Yang, Y.; Guo, M.; Zhang, G.; Li, W. Tuning the Electronic and Magnetic Properties of Porous Graphene-like Carbon Nitride through 3d Transition-Metal Doping. *Carbon* **2017**, *117*, 120–125.
- (52) Jun, Y. S.; Lee, E. Z.; Wang, X.; Hong, W. H.; Stucky, G. D.; Thomas, A. From Melamine-Cyanuric Acid Supramolecular Aggregates to Carbon Nitride Hollow Spheres. *Adv. Funct. Mater.* **2013**, 23, 3661–3667.
- (53) Chen, Z.; Zhang, J.; Zheng, S.; Ding, J.; Sun, J.; Dong, M.; Abbas, M.; Chen, Y.; Jiang, Z.; Chen, J. The Texture Evolution of g-C₃N₄ Nanosheets Supported Fe Catalyst During Fischer—Tropsch Synthesis. *Mol. Catal.* **2018**, 444, 90–99.
- (54) Yang, F.; Ren, J.; Liu, Q.; Zhang, L.; Chai, Y.; Dai, W. L. Facile Oxalic Acid-Assisted Construction of Laminated Porous *N*-Deficient Graphitic Carbon Nitride: Highly Efficient Visible-Light-Driven Hydrogen Evolution Photocatalyst. *J. Energy Chem.* **2019**, *0*, 1–8.
- (55) Luo, B.; Song, R.; Geng, J.; Jing, D.; Zhang, Y. Facile Preparation with High Yield of a 3D Porous Graphitic Carbon Nitride for Dramatically Enhanced Photocatalytic H₂ Evolution under Visible Light. *Appl. Catal., B* **2018**, 238, 294–301.
- (56) Kaniyoor, A.; Ramaprabhu, S. A Raman Spectroscopic Investigation of Graphite Oxide Derived Graphene. *AIP Adv.* **2012**, 2, 032183–032197.
- (57) Cançado, L. G.; Jorio, A.; Ferreira, E. H. M.; Stavale, F.; Achete, C. A.; Capaz, R. B.; Moutinho, M. V. O.; Lombardo, A.; Kulmala, T. S.; Ferrari, A. C. Quantifying Defects in Graphene *via* Raman Spectroscopy at Different Excitation Energies. *Nano Lett.* **2011**, *11*, 3190–3196.

(58) Thommes, M. Physical Adsorption Characterization of Nanoporous Materials. *Chem. Ing. Tech.* **2010**, 82, 1059–1073.

- (59) Fu, Y.; Zhu, J.; Hu, C.; Wu, X.; Wang, X. Covalently Coupled Hybrid of Graphitic Carbon Nitride with Reduced Graphene Oxide as a Superior Performance Lithium-Ion Battery Anode. *Nanoscale* **2014**, 6, 12555–12564.
- (60) Kruk, M.; Jaroniec, M. Gas Adsorption Characterization of Ordered Organic-Inorganic Nanocomposite Materials. *Chem. Mater.* **2001**, *13*, 3169–3183.
- (61) Hankel, M.; Searles, D. J. Lithium Storage on Carbon Nitride, Graphenylene and Inorganic Graphenylene. *Phys. Chem. Chem. Phys.* **2016**, *18*, 14205–14215.
- (62) Mao, Y.; Duan, H.; Xu, B.; Zhang, L.; Hu, Y.; Zhao, C.; Wang, Z.; Chen, L.; Yang, Y. Lithium Storage in Nitrogen-Rich Mesoporous Carbon Materials. *Energy Environ. Sci.* **2012**, *5*, 7950–7955.